Chemical Engineering Journal 468 (2023) 143553

Contents lists available at ScienceDirect

Chemical Engineering Journal

journal homepage: www.elsevier.com/locate/cej

Solar-driven gas phase photocatalytic CO_2 methanation by multimetallic UiO-66 solids decorated with RuO_x nanoparticles

María Cabrero-Antonino [a,1], Arianna Melillo [a,1], Eva Montero-Lanzuela [a], Mercedes Álvaro [a], Belén Ferrer [a], Ignacio Vayá [a,b], Herme G. Baldoví [a,*], Sergio Navalón [a,*]

[a] Departamento de Química, Universitat Politècnica de València, Camino de Vera s/n, Valencia 46022, Spain
[b] Instituto de Tecnología Química UPV-CSIC, Universitat Politècnica de València, Avenida de los Naranjos s/n, Valencia 46022, Spain

ARTICLE INFO

Keywords:
Heterogeneous catalysis
Metal–organic frameworks
multimetallic UiO-66 solids
CO_2 methanation
Simulated sunlight irradiation

ABSTRACT

As there is an urgent need to produce solar fuels from CO_2, we here report on the development of a series of multimetallic UiO-66(Zr/Ce/Ti) solids-supported RuO_x nanoparticles as photocatalysts for selective gas phase CO_2 methanation by H_2 under simulated sunlight irradiation. The trimetallic UiO-66(Zr/Ce/Ti) based-photocatalyst exhibits higher activity (1,900 μmol g^{-1} of CH_4 after 22 h) than analogous mono- [UiO-66(Zr) or UiO-66 (Ce)] and bimetallic [UiO-66(Zr/Ce) or UiO-66(Zr/Ti)] derivatives, as well as higher than previous reports on metal–organic frameworks (MOFs). The experimental evidence on the observed order of photocatalytic activity and insights into the occurrence of a dual photochemical and photothermal mechanism for the most active trimetallic sample were obtained by means of spectroscopic techniques including fluorescence and laser flash photolysis, photoelectrochemical and additional photocatalytic measurements. This study exemplifies the benefits of developing multimetallic MOF-supported metal nanoparticles to achieve high photocatalytic activity for solar-driven gas phase CO_2 conversion.

1. Introduction

More than 80 % of the worldwide energy demand is at present supplied by fossil fuels [1,2] whose combustion releases tens of GTons of CO_2 per year into the atmosphere [2,3], one of the main greenhouse gases responsible for global warming and climate change [1–5]. There is thus an urgent need to replace these fuels by sustainable and renewable energy vectors [6–12]. The ultimate goal of many countries is to develop technologies that favour the decarbonization of the energy sector [13–15]. For example, the European Union aims to be climate neutral by 2050 [16]. Carbon capture, usage and storage (CCUS) are envisioned as key technologies in achieving net-zero emissions [17–19]. Some studies have shown CO_2's potential use as sustainable feedstock for the chemical industry [14,20,21] as its high chemical stability means its transformation into chemicals an energy-intensive process. In this context, catalysis has reduced the activation energy required to reduce CO_2 to fuels and chemicals [14,20,22]. For example, several reports mainly using metal oxide-based catalysts have shown the possibility of performing selective gas-phase CO_2 reduction using H_2 to CH_4 and H_2O [2,23]. This catalytic process, known as the Sabatier reaction, is envisioned as a promising technology for large-scale CO_2 re-use. This methane can be transported and used for example as fuel in the existing natural gas facilities or to boost industrial decarbonization via synthetic natural gas technology [24,25]. The Sabatier reaction is a thermodynamically favourable exothermic process that can occur at temperatures as low as 25 °C [26–28]. However, CO_2 hydrogenation to CH_4, is a kinetically unfavourable eight-electron process and so typically requires high reaction temperatures (>300 °C) to achieve high efficiencies even when using metal nanoparticles (NPs) as co-catalysts [23]. RuO_x NPs are considered as one of the most active co-catalysts for photocatalytic CO_2 reduction and also are highly selective towards CH_4 [22]. In this context, the development of catalytic systems able to efficiently operate at room temperature is one of the challenges in this area [26,27]. Interestingly, some studies have reported the photocatalytic version of the Sabatier reaction under relatively mild reaction conditions (T < 200 °C and atmospheric pressure) [14]. Most of the active photocatalysts developed for this purpose include traditional metal oxides such as TiO_2 [28,29] and more recently other solids such as carbon-based materials like

* Corresponding authors at: Departamento de Química, Universitat Politècnica de València, Camino de Vera s/n, Valencia 46022, Spain.
E-mail addresses: hergarba@cam.upv.es (H.G. Baldoví), sernaol@doctor.upv.es (S. Navalón).
[1] Both are considered as first authors.

https://doi.org/10.1016/j.cej.2023.143553
Received 17 January 2023; Received in revised form 4 May 2023; Accepted 13 May 2023
Available online 16 May 2023

graphenes [30,31] and carbon nitride [32], perovskites [33] and metal–organic frameworks (MOFs) have also been used [34]. These supports act as photocatalysts when irradiated with wavelengths of appropriate energy via the so-called photochemical pathway with the generation of electrons and holes as the charge carriers responsible for the reduction and oxidation processes, respectively. Most of the photocatalysts reported for the Sabatier reaction also require finely dispersed metal or metal oxide NPs as co-catalysts such as RuO_x [29,35], Pd [33], Ni [31,32] or Cu [30,34], among other possibilities to enhance their activity. In addition to high activity and selectivity for RuO_x NPs as co-catalyst for CO_2 methanation, during the photocatalytic process they also enhance the resulting activity. Some of the factors in increasing their activity include their role of trapping photoinduced charge carriers and the intrinsic localized surface plasmon resonance of RuO_x, which favours the photothermal reaction pathway by transforming light energy into local heat [22,27,36–38]. Regardless of the achievements in this area, there is still a need for active photocatalysts that can efficiently operate under milder reaction conditions and natural solar light irradiation. It should be noted that some studies have reported that photocatalytic CO_2 reduction by H_2O can occur at ambient temperature while the photocatalytic CO_2 reduction by H_2 at moderate temperatures (~150 °C) has been proposed as a more efficient process [26].

Using MOFs for the photocatalytic Sabatier reaction is a relatively recent field of research. Some of their salient properties [39–41] that can contribute to this important area include their high versatility and tunability through a large number of possible combinations of organic ligands and secondary inorganic building units (SBU) to construct active and stable photocatalysts with unique energy level band diagrams, even under solar light irradiation [42–45]. In this context, Cabrero-Antonino et al. (2019) reported the first example of Zn-based MOF-supported Cu_2O (1 wt%) NPs as the heterogeneous photocatalyst for CO_2 methanation using H_2 under ultraviolet–visible (UV–Vis) irradiation at 215 °C [34]. Since then, other studies have also reported the use MOFs such as MIP-208(Ti) [46] or MIL-125(Ti)–NH_2 [36] supported RuO_x NPs with metal loadings from about 1 to 10 wt% as co-catalyst for solar-driven CO_2 methanation by H_2 at temperatures of about 200 °C. In general, the MOFs reported for this purpose are composed of a monometallic SBU bridged by one functionalized organic ligand [34,36,46]. Although several reports highlighted the possibility of using mixed-metal MOFs as efficient photocatalysts for different reactions, e.g. liquid phase CO_2 reduction in the presence of sacrificial agents [42,47], as far as we know this strategy has not yet been used for photocatalytic gas-phase CO_2 reduction by H_2. Among other possibilities offered by MOFs, UiO-66 materials are some of the most frequently studied mixed-metal MOFs with promising properties as photocatalysts [48,49]. More specifically, monometallic UiO-66(Zr) based-materials have been widely used as photocatalysts due to the combination of several factors including good porosity, stability and the possibility of enhancing their photoresponse and charge separation efficiency by rational design [49]. In this context, several studies have reported on boosting the photocatalytic activity of monometallic UiO-66(Zr) solid by preparing analogous materials based on mixed-metal UiO-66 solids with Zr(IV) metal nodes together with Ti (IV) or Ce(IV) ions [49]. Some of these studies [49–51] have reported that the enhanced photocatalytic activity of the mixed-metal UiO-66(Zr/Ti) or UiO-66(Zr/Ce) based photocatalysts is associated with their favourable overlapping between the highest occupied crystal orbital (HOCO) in the organic ligand with the lowest unoccupied crystal orbital (LUCO) of the metal nodes and narrow band gap resulting in a more efficient LMCT pathway [49,52,53]. Related studies using mixed-metal UiO-66(Zr/Ti)–NH_2 have proposed using Ti(IV) ions to act as mediators during the photoinduced electron transfer from the HOCO of the organic ligand to the metal node. The theoretical and experimental evidence achieved from this process is compatible with initial formation Ti (III)–O–Zr(IV) species in the metal node of the MOF and its further transformation into Ti(IV)–O–Zr(III) via metal–metal electron exchange [53,54].

In 2018, theoretical calculations indicated the possibility of using Ce-based UiO-66 solids as efficient photocatalysts with improved ligand-to-metal charge transfer (LMCT) pathways [55]. In fact, a recent study has reported that UiO-66(Ce)–NH_2 or UiO-66(Ce)–NO_2 are more active photocatalysts for the hydrogen evolution (HER) or oxygen evolution reaction (OER) than their analogous Zr-based UiO-66 solids [56]. However, the Ce-based MOFs suffer some metal leaching (~5 wt% respect to their initial amount present in the solids), while negligible metal leaching was measured in the case of Zr-based materials. Regardless of these comments, it is interesting to note that in 2018 it was also proposed by theoretical calculations that the photocatalytic activity of the UiO-66(Ce) materials can be further enhanced by preparing bimetallic UiO-66(Ce/Zr) or UiO-66(Ce/Ti) solids [52]. One of the main reasons given for the better photocatalytic response of these mixed-metal UiO-66 solids is their improved response in the visible region. It is also interesting to note that previous studies have reported that the possibility of developing mixed-metal MOFs in which one of the metals provides chemical stability while the other enhances catalytic activity. A similar situation might occur when using mixed-metal UiO-66 solids with stable Zr(IV) metal nodes [57]. In fact, a related precedent has shown that trimetallic UiO-66(Zr/Ce/Ti) is a stable material with better photocatalytic activity than UiO-66(Zr/Ce), UiO-66(Zr/Ti) or the monometallic UiO-66(Zr) or UiO-66(Ce) for the overall water splitting [51]. Transient absorption and photoluminescence measurements were used to propose that the improved activity of UiO-66(Zr/Ce/Ti) is due to its improved charge separation efficiency and therefore lower undesirable charge carrier recombination. Douhal and co-workers recently reported a comprehensive investigation on the influence of metal doping in mixed-metal amino functionalised UiO-66 solids on their photodynamics by using a series of spectroscopic measurements [50]. The series of MOFs include UiO-66(Zr)–NH_2, UiO-66(Ce)–NH_2, UiO-66(Zr/Ce)–NH_2, UiO-66(Zr/Ti)–NH_2 and UiO-66(Zr/Ce/Ti)–NH_2. The obtained spectroscopic and photocatalytic results indicated higher activity of bimetallic and especially the trimetallic UiO-66 solid due to the greater population of long-lived photoinduced charge carriers.

In this context, the present study reports on the development of multimetallic UiO-66 solids with Zr(IV) metal nodes together with Ce (IV) and/or Ti(IV) ions decorated with RuO_x NPs as benchmark co-catalyst for the photocatalytic solar-driven gas-phase CO_2 methanation by H_2. The MOF series include: UiO-66(Zr), UiO-66(Zr/Ce), UiO-66(Zr/Ti) and UiO-66(Zr/Ce/Ti) as well as UiO-66(Ce) and UiO-66(Ce/Ti) for the sake of comparison. Photocatalytic tests were performed under simulated solar irradiation to rank the activity of the UiO-66 supported RuO_x NPs. The stability of the most active material was evaluated by several reuse experiments and then characterizing the photocatalyst material use. The reaction mechanism during the photocatalytic reaction was studied by means of spectroscopic techniques such as fluorescence and laser flash photolysis (LFP) together with photocurrent measurements and specific photocatalytic experiments.

2. Experimental section

2.1. Materials

All the chemicals and solvents used in this study were of analytical or HPLC grade and obtained from Merck.

2.2. Catalyst preparation

The series of UiO-66(M: Zr, Ce, Zr/Ce, Zr/Ti, Zr/Ce/Ti) materials used in this study were all from the same batch, as previously reported [51]. For comparison, UiO-66(Ce/Ti) solid was prepared based on previous reports [58]. Table S1 summarises the atomic percentage of the metals present in these samples. These MOFs were loaded with RuO_x NPs by the photodeposition method [46]. Briefly, 50 mg of MOF were dispersed by sonication (450 W for 15 min) in a solution of Milli-Q water

(11 mL) and MeOH (5 mL) using a quartz tube. The corresponding amount of $KRuO_4$ dissolved in Milli-Q water (2 mL) was then added to the tube and sonicated for an additional 5 min and the system was purged with Ar for 20 min. The suspension under stirring was irradiated with a UV–Vis light lamp (150 W) for 4 h. The solid was recovered by filtration, washed several times with water and dried at 100 °C overnight. Before use, the sample was activated under vacuum at 150 °C for 12 h. Inductively coupled plasma atomic emission spectroscopy (ICP-AES) analyses of the liquid phase used during photodeposition after removing the methanol under vacuum at 40 °C revealed the absence of ruthenium in solution. Digestion of the RuO_x NPs supported UiO-66 solids (20 mg) in aqua regia (25 mL) under reflux for 8 h and analysis of the liquid phase by ICP-AES confirmed the full incorporation of the ruthenium (1 wt% respect to the MOF) initially added as $KRuO_4$. The selection of this co-catalyst loading was for the sake of comparison with previous similar studies that reported that RuO_x NPs with a ruthenium final loading of about 1 wt% within the MOF is an adequate strategy to enhance photocatalytic CO_2 reduction by H_2 at temperatures of about 200 °C [36,46].

2.3. Characterization of the materials

The MOF-based materials were characterized by powder X-ray diffraction (PXRD), spectroscopic techniques including: UV–Vis diffuse reflectance spectroscopy (UVDRS), X-ray photoelectron spectroscopy (XPS), laser flash photolysis (LFP) and photoluminescence (PL) spectroscopy, scanning (SEM) and transmission (TEM) electron microscopies equipped with energy-dispersive X-ray (EDX) detector or photocurrent measurements. The experimental details of the characterization techniques can be seen in the Supplementary Material.

2.4. Photocatalytic reactions

All the photocatalytic reactions were carried out at least in triplicate. The photocatalytic data is that of the average value of at least three independent experiments. Briefly, the required amount of MOF (15 mg) was placed in a quartz reactor (51 mL) equipped with a heating mantle and thermocouple connected to a controller that set the reaction temperature [36]. The system was then purged with H_2 for 20 min and CO_2 was introduced to obtain a H_2:CO_2 ratio 4:1 and 1.3 bar total pressure. The system was then heated to the required temperature (*i.e.* 200, 175, 150 or 125 °C) and the photocatalyst placed on the bottom of the reactor was irradiated by a commercially available Hg-Xe lamp (150 W, Hamamatsu ref. L8253; Hamamatsu spot light source L9566-04 and light guide A10014-50–0110) with or without a commercially available AM 1.5G type filter (Lasing ref. 81094) to obtain simulated sunlight irradiation. In some cases, commercially available transmittance filters (Newport, ref. FSQ-OD30, FSQ-OD15 or FSQ-QD05) were also used to study the influence of radiation intensity on the photocatalytic activity. The evolution of the reaction was followed by analysing reaction aliquots in an Agilent 490 MicroGC equipped with a thermal conductivity detector and two channels, one with a MolSieve 5A column to analyse H_2, O_2, N_2, and CO, while the other had a Pore Plot Q column to analyse the CO_2, CH_4, and short-chain hydrocarbons. Quantification was by calibration plots with commercially available gas mixtures.

3. Results and discussion

3.1. Photocatalyst preparation and characterization

The crystallinity of UiO-66(Zr), UiO-66(Ce), UiO-66(Zr/Ce), UiO-66 (Zr/Ti) and UiO-66(Zr/Ce/Ti) supported RuO_x NPs was first studied by PXRD. Fig. 1a shows that all these materials are crystalline with UiO-66 topology after the deposition of RuO_x NPs [59]. In good agreement with previous reports [51,60], the small but significant shift in the UiO-66 (Ce) diffraction peaks with respect to the other samples is attributable

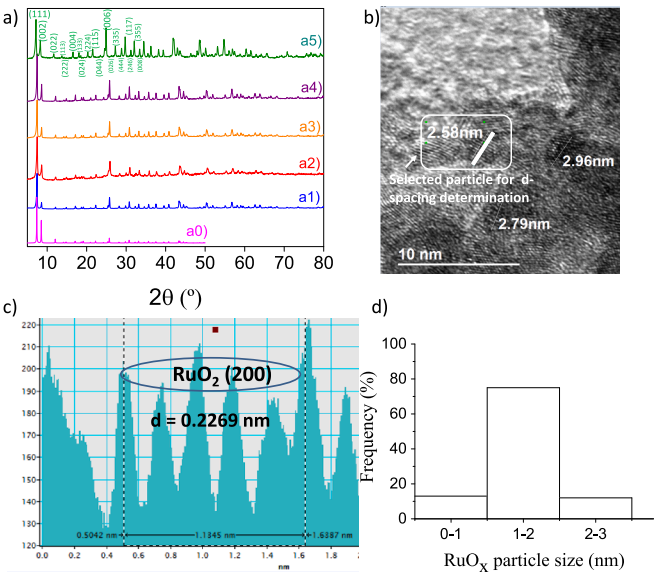

Fig. 1. (a) XRD of simulated uio-66 (a0) and PXRD of RuO_x NPs supported UiO-66 samples. Legend: a0) simulated UiO-66; (a1) UiO-66(Zr), (a2) UiO-66(Zr/Ti), (a3) UiO-66(Zr/Ce), (a4) UiO-66(Zr/Ce/Ti), (a5) UiO-66(Ce) and Miller indices. (b) Representative HR-TEM image of RuO_x@UiO-66(Zr/Ce/Ti). (c) Peak intensity versus interplanar distance graph from selected particle in panel (a) associated to the RuO_2 (200) planes. (d) Particle size distribution of RuO_x NPs supported on UiO-66(Zr/Ce/Ti). Note: the average particle size of RuO_x NPs supported on UiO-66(Zr/Ce/Ti) was 1.49 nm.

to the higher ionic radii of Ce(IV) *vs.* Zr(IV) or Ti(IV), which results in a contraction of the unit cell. Also, the relatively higher peak intensities of UiO-66(Ce) than the other samples can be attributed to its higher crystallinity. The absence of additional diffraction peaks after RuO_x NPs loading by the photodeposition method can be attributed to the good dispersion of small RuO_x NPs and/or the low ruthenium loading (1 wt%; section 2.2). Fig. 1b shows a representative high-resolution TEM (HR-TEM) image of RuO_x@UiO-66(Zr/Ce/Ti) together with d-spacing analysis (Fig. 1c) confirming the presence of small RuO_x NPs (Fig. 1d). The series of the samples were also characterized by HR-TEM and dark-field scanning TEM (DF-STEM) measurements coupled to the EDX detector and, thus, confirming a similar average RuO_x particle size and standard deviation with values around 1.46 ± 0.03 nm, respectively (Fig. 1 and Figs. S1–S5). Characterization of RuO_x NPs supported UiO-66 solids by high-resolution SEM (HR-SEM) also coupled to the EDX detector confirms a good distribution of the elements within the MOF particle (Figs. S6–S10).

The series of UiO-66 supported RuO_x NPs were also characterized by XPS (Fig. 2 and Figs. S11–S14). Fig. 2a shows the XPS C 1 s and Ru 3d spectra partially overlapped, although two main bands can be distinguished at 284.4 and 292 eV associated with the C-C sp^2 bonding and carboxylate groups present in the terephthalate ligand of the MOF, respectively. The less intense signal centred at 281.2 eV can be assigned to Ru $3d_{3/2}$ in the form of RuO_2 or hydrated species [61,62]. The relatively weak Ru 3d signal can be attributed to the low ruthenium loading on the catalyst, in good agreement with previous reports [36]. XPS C 1 s + Ru 3d comparison of RuO_x@UiO-66(Zr/Ce/Ti) and pristine UiO-66 (Zr/Ce/Ti) (Fig. S15) indicates that the weak signal at about 281.7 eV in the RuOx@UiO-66(Zr/Ce/Ti) sample can be associated with the presence of RuO_x NPs. In the case of the RuO_x@UiO-66(Ce) sample, the XPS Ru 3p spectrum shows two bands centred at 484.5 and 462.2 eV associated with the presence of RuO_x NPs in agreement with the XPS Ru 3d (Fig. S12). The XPS O 1 s spectrum shows a broad band due to the presence of oxygen atoms in the carboxylate groups (531 eV) together with the oxygen atoms present in the MOF metal cluster and ruthenium oxide species (529 eV). The XPS Zr 3d shows characteristic Zr(IV) bands

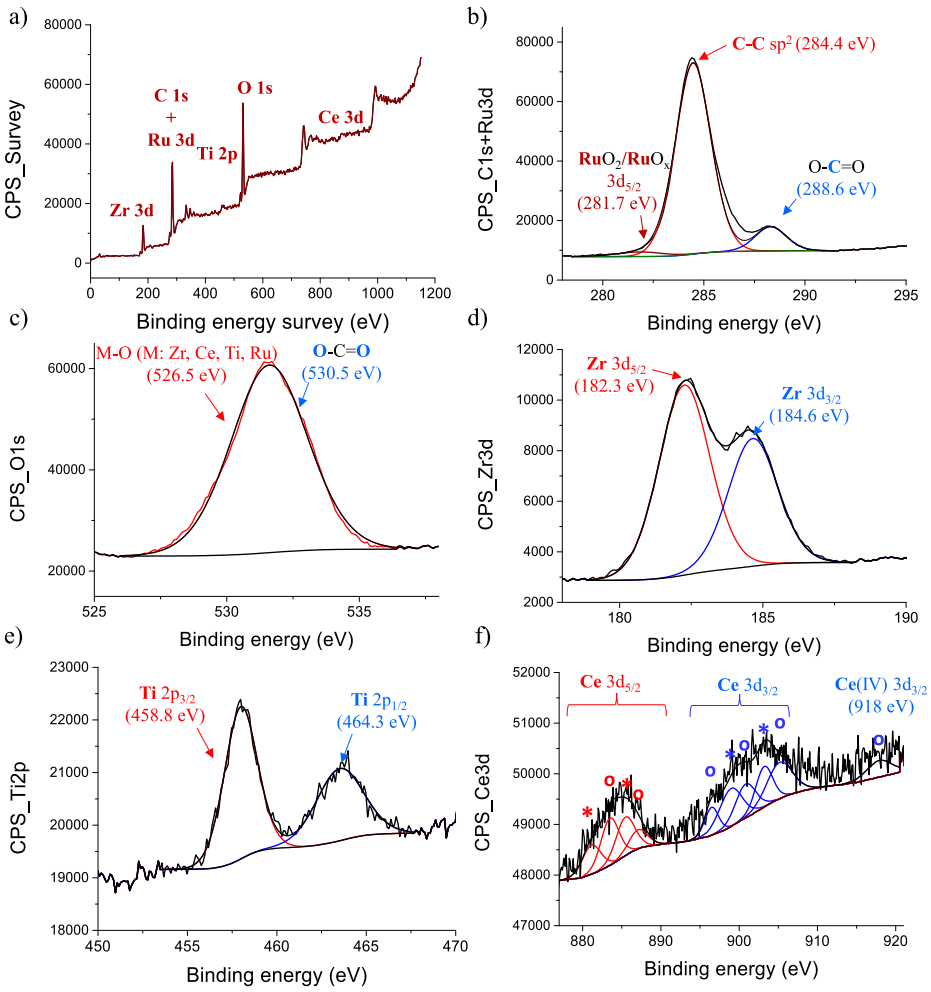

Fig. 2. XPS survey (a), C 1 s + Ru 3d (b), O 1 s (c), Zr 3d (d), Ti 2p (e) and Ce 3d (f) spectra of fresh UiO-66(Zr/Ce/Ti) supported RuO_x NPs.

at about 182 and 185 eV attributable to Zr $3d_{3/2}$ and Zr $3d_{5/2}$, respectively. The presence of Ti(IV) is confirmed by XPS Ti 2p with characteristic bands at about 455 and 462 eV for Ti $2p_{3/2}$ and Ti $2p_{1/2}$, respectively. The broad XPS Ce 3d bands appearing between 880 and 920 eV can be deconvoluted and assigned to the presence of the Ce(IV) and Ce(III) species [51].

The energy level diagrams of the UiO-66 solid-supported RuO_x NPs (Fig. 3) were estimated by means of UV–Vis diffuse reflectance spectroscopy (UV–Vis DRS) and XPS. Initially, the Tauc plot was used to estimate the optical band gap energy values from the UV-Vis DRS data (Fig. S16). The RuO_x@UiO-66(Ce) and RuO_x@UiO-66(Zr) solids exhibit the smallest and highest optical band gap energy values of the series,

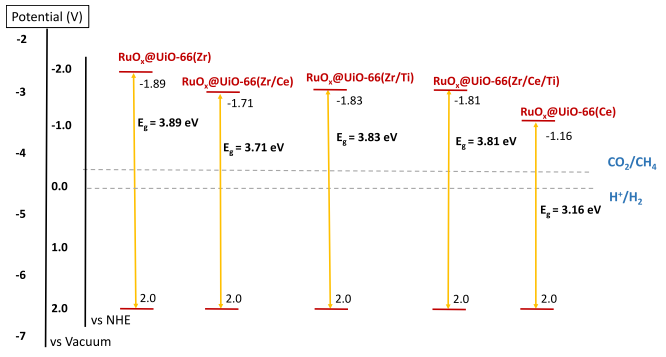

Fig. 3. Energy level diagram of UiO-66 solids supported RuO_x NPs.

with values between 3.16 and 3.89 eV, respectively. This observation is in good agreement with previous experimental [63,64] and theoretical calculations that predicted that the presence of low-lying empty 4f orbitals of Ce(IV) in UiO-66 solid would reduce the band gap and also favour the LMCT mechanism from the organic ligand to the metal node, with respect to the wide band gap UiO-66(Zr) solid [55]. The bimetallic RuO_x@UiO-66(Zr/Ce) or RuO_x@UiO-66(Zr/Ti) and the trimetallic RuO_x@UiO-66(Zr/Ce/Ti) also resulted in a red shift absorption with respect to the parent UiO-66(Zr) material. These observations also agree with previous studies showing the reduction of the band gap in the UiO-66(Zr) solids by the simultaneous presence of Ti(IV) or Ce(IV or III) ions [51,52]. XPS was further used to estimate the valence band maximum of the UiO-66 solids supported RuO_x NPs (Fig. S17). The energy level diagrams of the solids were determined from the XPS valence band maximum values and the optical band gaps obtained by the Tauc plots (see Fig. 3); further details can be obtained in the Supplementary Material.

3.2. Photocatalytic results

In the next step, the photocatalytic activity of the RuO_x NPs supported UiO-66 samples was studied for CO_2 reduction by H_2. Photocatalytic control experiments using UiO-66(Zr), UiO-66(Ce), UiO-66(Zr/Ce), UiO-66(Zr/Ti) and UiO-66(Zr/Ce/Ti) in the absence of RuO_x NPs as co-catalyst resulted in the formation of methane traces with the values of 6, 12, 17, 22 and 28 μmol g^{-1} after 22 h, respectively, while the presence of RuO_x NPs at 1 wt% loading within the UiO-66 solids greatly increased

methane production (Fig. 4a). It should be noted that in all cases methane was the only product detected during the photocatalysis. As it can be seen in Fig. 4a, the trimetallic UiO-66(Zr/Ce/Ti) supported RuO_x NPs sample showed the highest photocatalytic activity of the samples under study, achieving a CH_4 production as high as 1900 μmol g^{-1} and a CO_2 conversion of about 5.3 % after 22 h under simulated sunlight irradiation. The photoactivity decreased for the RuO_x NPs supported within the bimetallic UiO-66(Zr/Ti) and UiO-66(Zr/Ce) solids and decreased further for the UiO-66(Ce) and UiO-66(Zr) supported RuO_x NPs. As mentioned above, all five RuO_x NPs supported UiO-66 photocatalysts had a very similar RuO_x particle size distribution (Figs. S1–S4), the changes found in their activity can be associated with the metal node composition of the UiO-66 samples. Some relatively recent studies have reported the possibility of preparing bimetallic UiO-66(Ce/Ti) based-materials and used for (photo)catalytic applications [58,65]. In this context, RuO_x NPs (1.46 nm) supported on UiO-66(Ce/Ti) was prepared and characterised (Figs. S18, S19). The activity of this photocatalyst showed a CH_4 production of 1,150 μmol g^{-1} after 22 h under the conditions employed in Fig. 4.

A control experiment showed that the activity of the most active RuO_x@UiO-66(Zr/Ce/Ti) sample during the photocatalytic CO_2 methanation at 200 °C under simulated solar light irradiation (0.082 mmol g^{-1} after 22 h) was more than double that of a similar experiment under dark conditions (0.037 mmol g^{-1} after 22 h). The fact that the RuO_x@UiO-66(Zr/Ce/Ti) sample was active in a dark reaction is not unexpected, since ruthenium species are some of the most active sites for CO_2 hydrogenation [22]. As it is discussed below, photocatalytic CO_2 reduction by RuO_x@UiO-66(Zr/Ce/Ti) takes place through a dual photochemical and photothermal mechanism in which light irradiation promotes a photoinduced charge separation and converts it into heat energy, respectively. However, photocatalytic CO_2 methanation under simulated sunlight is an appealing process in which the reaction can take place under milder reaction conditions than the thermal catalytic process. With these considerations in mind, we further proceeded to study the influence of the reaction temperature on photocatalytic CO_2 methanation by RuO_x@UiO-66(Zr/Ce/Ti). As can be seen in the inset of Fig. 4b, photocatalytic methane generation increased with the reaction temperature in accordance with Arrhenius' law. The apparent activation energy for CO_2 hydrogenation to methane was estimated to be 29 kJ/mol from these photocatalytic data. This value compares favourably with similar studies with RuO_x NPs at 10 wt% loading supported on MIL-125(Ti)–NH_2, also for CO_2 methanation, a process with an estimated activation energy of 68.8 kJ/mol [36]. This result again highlights the importance of the proper metal node composition in UiO-66(Zr/Ce/Ti) to favour the kinetics of photocatalytic CO_2 methanation, even when working with a relatively low ruthenium loading (1 wt%).

To put the results obtained into context, the photocatalytic activity of the most active RuO_x@UiO-66(Zr/Ce/Ti) material was compared with that achieved using a previously reported different MOF-based catalyst (Table 1). In previous studies, the use of RuO_x NPs as co-catalyst at ~ 1 wt% supported on Ti-MOFs, namely MIL-125(Ti)–NH_2 [36] or MIP-208 (Ti) [46], resulted in around half the methane-generating photocatalytic activity of that achieved using UiO-66(Zr/Ce/Ti). Also remarkable is the fact that the photocatalytic activity of RuO_x@UiO-66(Zr/Ce/Ti) is similar to that achieved when using MIL-125(Ti)–NH_2 supported RuO_x NPs at 2 wt% [36]. Furthermore, the photocatalytic activity achieved with RuO_x@UiO-66(Zr/Ce/Ti) at 175 °C (864 mmol g^{-1} at 22 h) is similar to that obtained by a similar process with RuO_x@MIP-208(Ti) at 200 °C [46]. For comparison, the photocatalytic activity of this material was also tested under UV–Vis irradiation and, as expected, was found to be higher than simulated sunlight irradiation (Table 1, entry 1 *vs.* 2). All these findings are important since they highlight the possibility of tuning UiO-66(Zr) metal node composition by using non-toxic and highly available transition metals such as Ti(IV) or Ce(IV) in a way that obtains active solar-driven photocatalysts at relatively low reaction temperatures.

An important aspect to consider when performing (photo)catalytic CO_2 reduction reactions is to demonstrate that the reaction obtained products from CO_2. A widely used strategy to confirm this, is to use isotopically labelled $^{13}CO_2$ to form ^{13}C labelled reaction products. In the present case, the photocatalytic reaction used $^{13}CO_2$ and RuO_x@UiO-66 (Zr/Ce/Ti) with the gas phase injected in a GC–MS. Fig. S20 shows the mass spectrum of the injected gas that was obtained, and confirmed the presence of *m/z* 17 from the molecular ion of $^{13}CH_4$. It should be noted that control experiments carried out before the reaction did not reveal the presence of this *m/z* peak (data not shown).

The reusability of the most active RuO_x@UiO-66(Zr/Ce/Ti) was evaluated for photocatalytic CO_2 methanation under simulated solar irradiation by reusing it four consecutive times. In Fig. 5a it can be seen that the photocatalytic activity is practically maintained during the four consecutive catalytic cycles. The crystallinity of the four-times used photocatalyst is retained as revealed by PXRD (Fig. 5b). TEM measurements of the four-times used RuO_x@UiO-66(Zr/Ce/Ti) indicated that the RuO_x average particle size (1.51 nm) is comparable to that of the fresh sample (1.49 nm), while no significant aggregation of the used material was detected (Fig. 5c,d). As previously shown in Fig. 1b and 1c,

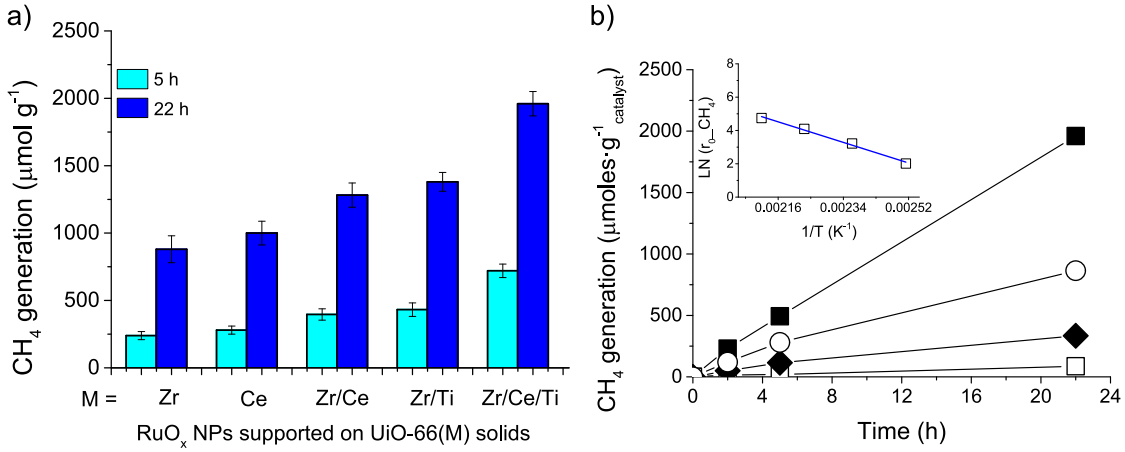

Fig. 4. (a) Photocatalytic CH_4 generation using RuO_x NPs supported on UiO-66 solids under simulated sunlight irradiation at 200 °C. (b) Influence of the reaction temperature on photocatalytic CH_4 generation using RuO_x@UiO-66(Zr/Ce/Ti) under simulated sunlight irradiation. Legend: 125 (□), 150 (◆), 175 (○) and 200 (■) °C. The inset shows the Arrhenius' plot of the data obtained. Note: The photocatalytic data presented in these plots corresponds to three independent experiments. Reaction conditions: Photocatalyst (15 mg), $P_{H2} = 1.05$ bar, $P_{CO2} = 0.25$ bar, reaction temperature as indicated, simulated sunlight irradiation (Hg-Xe lamp of 150 W equipped with an AM 1.5G type filter).

Table 1
Photocatalytic CO_2 methanation by H_2 using heterogeneous materials reported in the literature compared with those prepared in this study.[a.]

Entry	Photocatalyst	Co-catalyst	Irradiation source	Reaction conditions	CH_4 production (mmol $g^{-1}h^{-1}$)	Ref.
1	UiO-66(Zr/Ce/Ti)	RuO_x (1 wt%)	Simulated solar light irradiation (150 W Hg-Xe lamp equipped with an AM 1.5 filter)	P_{H2} = 1.05 bar, P_{CO2} = 0.25 bar, 200 °C, 22 h	0.082	This work
2	UiO-66(Zr/Ce/Ti)	RuO_x (1 wt%)	UV–Vis light irradiation (150 W Hg-Xe lamp)	P_{H2} = 1.05 bar, P_{CO2} = 0.25 bar, 200 °C, 22 h	0.13	This work
3	MIP-208(Ti)	RuO_x (0.76 wt%)	Simulated solar light irradiation (150 W Hg-Xe lamp equipped with an AM 1.5 filter)	P_{H2} = 1.05 bar, P_{CO2} = 0.25 bar, 200 °C, 22 h	0.036	[46]
4	MIL-125 (Ti)–NH_2	RuO_x (1 wt%)		P_{H2} = 1.05 bar, P_{CO2} = 0.25 bar, 200 °C, 22 h	0.042	[36]
5	MIL-125(Ti)–NH_2	RuO_x (2 wt%)	Simulated solar light irradiation (150 W Hg-Xe lamp equipped with an AM 1.5 filter)	P_{H2} = 1.05 bar, P_{CO2} = 0.25 bar, 200 °C, 22 h	0.1	[36]
6	MIL-125(Ti)–NH_2	RuO_x (10 wt%)		P_{H2} = 1.05 bar, P_{CO2} = 0.25 bar, 200 °C, 22 h	0.84	[36]
7	MOF-Zn(1)	Cu_2O (1 wt %)	UV–Vis light irradiation (300 W Xe lamp)	P_{H2} = 1.05 bar, P_{CO2} = 0.25 bar, 215 ºC 24 h	0.0019	[34]

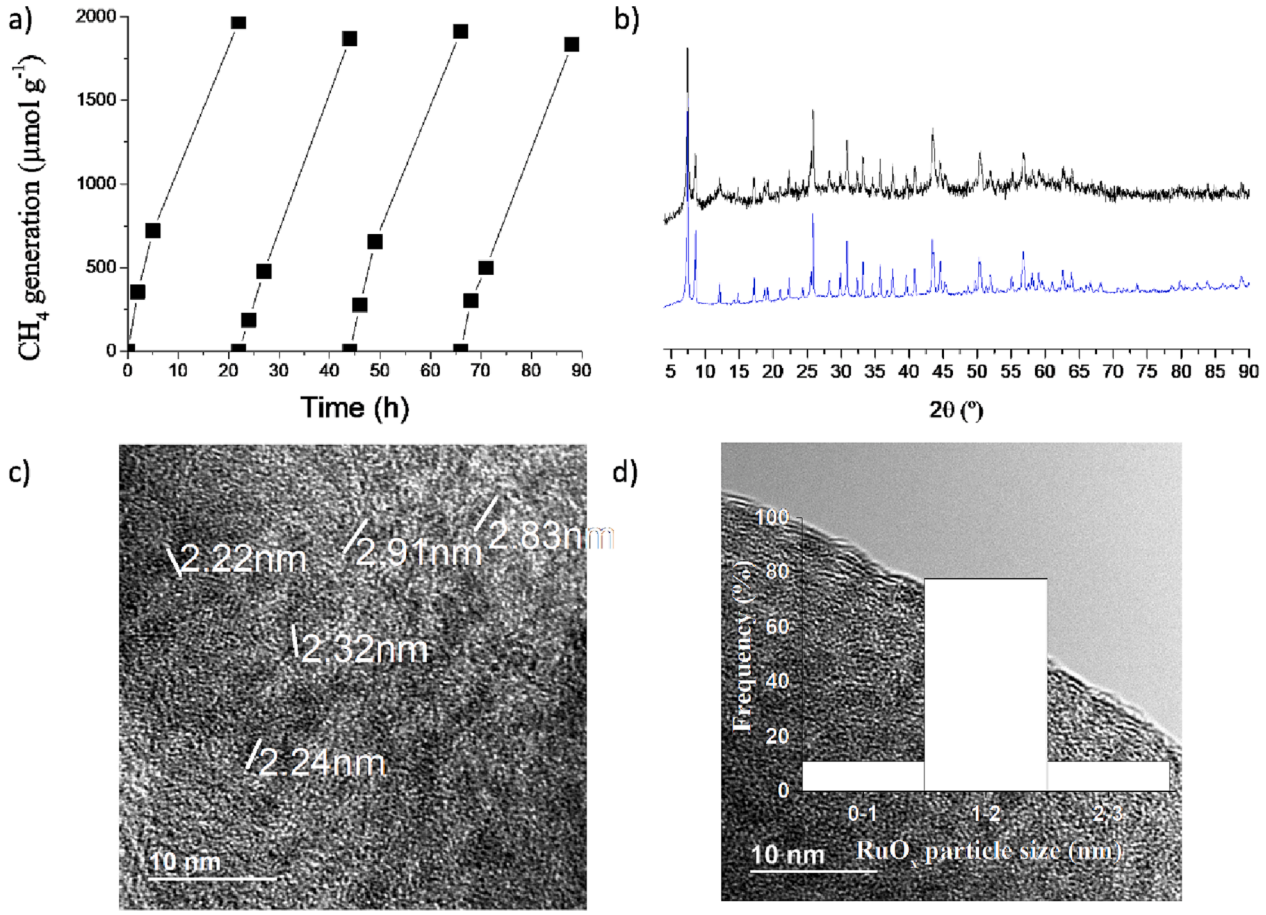

Fig. 5. (a) Reusability of RuO_x@UiO-66(Zr/Ce/Ti) during the photocatalytic CO_2 methanation. Photocatalyst (15 mg), P_{H2} = 1.05 bar, P_{CO2} = 0.25 bar, reaction temperature 200 °C, simulated sunlight irradiation (Hg-Xe lamp of 150 W equipped with an AM 1.5G filter). Note: The photocatalytic data corresponds to three independent experiments. (b) PXRD of the fresh and four-times used RuO_x@UiO-66(Zr/Ce/Ti) photocatalyst. (c) TEM image of fresh RuO_x@UiO-66(Zr/Ce/Ti). (d) TEM image and RuO_x NP size distribution of four-times used RuO_x@UiO-66(Zr/Ce/Ti).

d-spacing analysis from a HR-TEM image of fresh RuO_x@UiO-66(Zr/Ce/Ti) sample confirmed the presence of RuO_x NPs. Fig. S21 shows a representative DF-STEM image together with EDX analyses and a TEM image and d-scaping analysis confirming the presence of RuO_x NPs supported on the four-times used photocatalyst. In spite of this, some of the present authors reported in a previous study that a series of carboxylate-based MOF can suffer partial decarboxylation under exposure to UV–Vis irradiation. To confirm this finding, the optimized RuO_x@UiO-66(Zr/Ce/Ti) sample was submitted to simulated sunlight irradiation at 200 °C in an Ar atmosphere for 22 h. The results showed about 1.9 mol % decarboxylation of the RuO_x@UiO-66(Zr/Ce/Ti) sample, in agreement with previous reports (2.1 mol%) for RuO_x(10 wt %)@MIL-125(Ti)–NH_2, which suggests the need for more stable MOF-based photocatalysts for this purpose.

The four-times used RuO_x@UiO-66(Zr/Ce/Ti) photocatalyst was also characterized by XPS (Fig. 6 and S22). The most remarkable difference

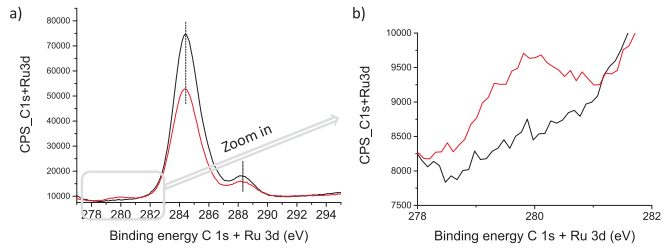

Fig. 6. (a) XPS C 1 s + Ru 3d of fresh and four times used RuO_x@UiO-66(Zr/Ce/Ti) and (b) zoom of the selected area highlighted in grey colour.

between the used and the fresh samples was finding a new XPS band centred at 279.8 eV for the former. This band can be associated with Ru $3d_{3/2}$ species that at least partially reduced the RuO_x present in the fresh catalyst during the photocatalytic CO_2 reaction at 200 °C in an H_2 atmosphere. Similar conclusions were obtained by means of *in situ* XPS experiments in which the fresh RuO_x@UiO-66(Zr/Ce/Ti) sample was submitted to H_2 treatment at 200 °C for 1 h. The results shown in Fig. S23 indicate that RuO_x NPs (Ru 3 $d_{5/2}$ 281.7 eV) supported in fresh UiO-66(Zr/Ce/Ti) are also present in the H_2 treated sample together with a new band at 279.6 eV, also associated with the presence of metallic Ru(0) species. Characterization of the ruthenium oxidation state by XPS Ti 2p shows a band at 484.9 eV due to RuO_x NPs in the fresh sample that is partially shifted to lower binding energies (483.4 eV) together with a new band centred at 460.7 eV. These XPS Ti 2p observations also reinforce the conclusion that the H_2 treated fresh photocatalyst exhibits a partial reduction, resulting in a sample with both oxidized and metallic ruthenium species [33,36]. Regardless of these comments, it should be mentioned that due to Ru 3d and 3p overlapping with the C 1 s and Ti 2p XPS, respectively, it is difficult to reach a clearer conclusion on the exact ruthenium oxidation state before and after the photocatalytic reaction using this technique.

3.3. Reaction mechanism

Previous studies have proposed that heterogeneous catalytic CO_2 methanation by H_2 can proceed mainly through three reaction pathways termed as direct CO_2 dissociation, reverse water gas shift reaction or formate pathway [27,66]. Fig. S24 shows the proposed reaction pathways according to these studies [66]. In general, selectivity towards CH_4 depends on the strength of reaction intermediates like CO or H_2COH/H_3CO close to the hydrogenation active sites. The stronger adsorption of the reaction intermediates favours CO_2 hydrogenation to CH_4. The reader is referred to some existing reviews on this topic for more details [22,27]. In fact, several studies on heterogeneous (photo)catalytic CO_2 reduction have reported that the formation of CH_4 is sometimes accompanied by other products like CO [26,27]. *In situ* FT-IR spectroscopy using CO as probe molecule is often used to understand the selectivity of CO_2 (photo)reduction to CH_4, which can differentiate vibration frequencies of CO physisorbed or chemisorbed on the catalyst [36,67,68]. In general, the presence of adsorption sites in the catalyst that favour CO chemisorption provides results in higher selectivities towards CH_4 formation than the catalysts with weakly physisorption sites [27].

As commented in the photocatalytic results, in the present study CH_4 was the only reaction product found. To obtain information on the high CH_4 selectivity achieved by the most active RuO_x@UiO-66(Zr/Ce/Ti) photocatalyst, an *in situ* CO adsorption FT-IR spectroscopy study was performed. Prior to these measurements, the solid was activated in the FT-IR chamber at 150 °C under vacuum for 4 h to remove possible adsorbed water molecules, and then the CO was dosed. The results are summarized in Fig. S25; the FT-IR spectrum shown by the blue line, which gives the results obtained after MOF saturation with CO, is characterized by two main bands appearing at 2171 and 2154 cm^{-1} associated with vibration frequencies of linearly chemisorbed CO on RuO_x NPs, as previously reported [67,68]. The system was then evacuated and the FT-IR spectrum recorded. The results show reduced intensities of the two main bands with a small shift of their maximum centred wavenumbers. These data suggest the presence of relatively strongly coordinated CO molecules to RuO_x NPs even after evacuation. The experiments indicate that the high selectivity found during photocatalytic CO_2 reduction is associated with the coordination of CO reaction intermediates or those similar to the RuO_x NPs, in which hydrogenation towards CH_4 takes place.

Another important point to address when investigating the photocatalytic CO_2 reduction process is to detect the possible occurrence of a dual photochemical and photothermal reaction mechanism [27]. In the photochemical mechanism, light irradiation with adequate energy induces the generation of electrons and holes responsible for the reducing and oxidising reactions, respectively. In contrast, in the photothermal mechanism, the light energy is transformed into heat, favouring the thermocatalytic process.

In the area of MOFs as photocatalysts including UiO-66 solids, the photochemical mechanism is commonly described via photoinduced LMCT. In this process, irradiation of the MOF with the appropriate wavelength, transfers photoinduced electrons from the organic ligand to the metal node. In 2018, theoretical calculations indicated that higher efficiency would be achieved via the LMCT mechanism on UiO-66(Ce) than with UiO-66(Ti) or even the inefficient UiO-66(Zr) [55,69,70]. It should be noted, however, that the preparation procedure to obtain the UiO-66(Ti) solid has not been experimentally reported yet as far as we know. In the present study, several photochemical and spectroscopic experiments were carried out to address the occurrence of this LMCT for the series of RuO_x-supported UiO-66 solids. It should be remembered that depositing RuO_x NPs within the MOF structure has been carried out using the photodeposition method consisting on irradiation of a methanol aqueous solution $KRuO_4$ by UV–Vis in the presence of suspended UiO-66 solids. These observations are indirect evidence of the occurrence of photoinduced charge separation in which photogenerated electrons and holes are responsible for RuO_x NP formation and methanol oxidation, respectively.

Previous reports have shown that the presence of metal or metal-oxide NPs can favour the LMCT mechanism by at least partially avoiding electron-hole recombination so that it favours photocatalytic processes [36,64]. As previously shown in Fig. 6 and S23, the RuO_x NPs supported on UiO-66 (Zr/Ce/Ti) in the fresh photocatalyst are reduced to some extent to metallic Ru(0) or partially reduced RuO_x NPs during photocatalytic CO_2 reduction by H_2 at 200 °C, as indicated by XPS. To consider the possible influence of the ruthenium oxidation state on the reaction mechanism, PL and LFP measurements were carried out using both the fresh and used RuO_x NPs supported UiO-66 solids. The PL responses of both Ar-purged fresh (Fig. 7a) and used (Fig. S26) MOF suspensions were initially measured in acetonitrile with the same absorbance at λ_{exc} = 266 nm (*ca.* 0.3), where the organic ligand is mainly excited. Fig. 7a shows that RuO_x@UiO-66(Zr) displayed the highest emission of the studied samples. The PL emission is lower for bimetallic UiO-66(Zr/Ti) or UiO-66(Zr/Ce), and especially trimetallic UiO-66(Zr/Ce/Ti) supported RuO_x NPs. Similar results, *i.e.* quenching of the observed fluorescence for bi- or trimetallic UiO-66 solids with respect to the parent MOF, were found for used RuO_x NPs supported UiO-66 solids (Fig. S26). These results agree with previous theoretical and experimental studies on the higher efficiency of the LMCT mechanism due to the presence of bimetallic or trimetallic UiO-66 solids. In other words, the higher PL quenching is assigned to a better photoinduced charge carrier separation. PL emission of pristine UiO-66(Zr/Ce/Ti) was also quenched by the presence of RuO_x NPs (Fig. 7b), which further supports the benefits of these metal NPs in favouring the LMCT mechanism.

Photocurrent measurements for the series of RuO_x NPs supported UiO-66 were carried out to evaluate the photoinduced charge separation

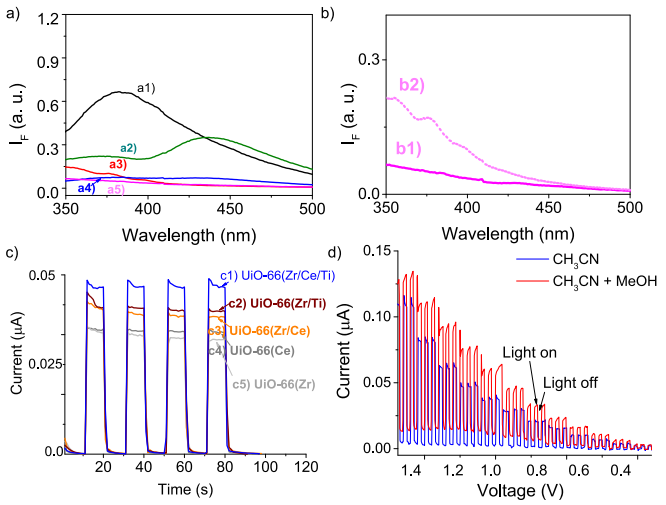

Fig. 7. (a) PL spectra (λ_{exc} = 266 nm) for fresh RuO_x NPs supported on UiO-66 (Zr) (a1), UiO-66(Zr/Ti) (a2), UiO-66(Ce) (a3), UiO-66(Zr/Ce) (a4) or UiO-66 (Zr/Ce/Ti) (a5) in Ar-purged acetonitrile. (b) Comparison of the PL obtained using RuO_x@UiO-66(Zr/Ce/Ti) (b1) and pristine UiO-66(Zr/Ce/Ti) (b2). (c) Current intensity of a FTO counter electrode supported RuO_x@UiO-66(Zr/Ce/Ti), RuO_x@UiO-66(Zr/Ti), RuO_x@UiO-66(Zr/Ce), RuO_x@UiO-66(Ce) or RuO_x@UiO-66(Zr) polarized at 0.9 V under Ar-purged acetonitrile solutions (tetra-*n*-butylammonium hexafluorophosphate, $TBAPF_6$, 0.1 M) and consecutive light on/off cycles using UV–Vis light. (d) Current intensity *vs.* polarization potential of an FTO counter electrode supported fresh RuO_x@UiO-66(Zr/Ce/Ti) under Ar-purged acetonitrile solutions ($TBAPF_6$, 0.1 M) in the absence (blue line) or in the presence (red line) of methanol (0.3 mL) under consecutive light on/off cycles using UV–Vis light.

efficiency on illumination (Fig. 7c). For this, a working electrode of fluoride-doped tin oxide (FTO) as transparent electrode polarized at 0.9 V containing RuO_x NPs supported UiO-66 material was submitted to several consecutive cycles of on/off light irradiation. The higher photocurrent intensity was achieved by RuO_x NPs supported UiO-66(Zr/Ce/Ti) followed by the bimetallic solids UiO-66(Zr/Ti) and UiO-66(Zr/Ce) and then UiO-66(Ce) and UiO-66(Zr). Interestingly, this photocurrent intensity order is the same as the one for the photocatalytic activities of these materials, and thus highlights the importance of mixed-metal nodes in UiO-66 solids to improve both charge separation efficiency and photocatalytic activity. In this context, photocurrent measurements were performed for RuO_x@UiO-66(Zr/Ce/Ti) using FTO as transparent electrode (polarization from 1.4 to 0.3 V and five consecutive cycles of on/off light irradiation at each polarized potential; see Fig. 7d). The results confirm higher current intensity due to the irradiation associated with photoinduced charge separation. In a similar experiment using methanol as sacrificial electron donor doubled the obtained current intensity (Fig. 7b, red line). This enhanced photocurrent in the presence of methanol is in good agreement with its role as electron donor to quench the photogenerated holes, thus increasing the population of the electrons responsible for raising the current intensity. Besides, it is interesting to note that once the light is turned on, the recorded photocurrent shows a slight gradual increase of intensity in the presence of methanol, while a gradual decrease of photocurrent intensity is observed in the case of using only acetonitrile. It should be noted that the first prompt step during the photocurrent measurement upon illumination is related with the charge separation process. Then, during the light pulse at longer times photochemical processes take place. In this scenario, the presence of methanol as electron donor favours upon irradiation both the efficiency of charge separation and accumulation of electrons and ions at the electrode surface, while in the absence of MeOH without the occurrence of photochemical reactions electron/hole pair recombination is favoured.

Previous reports have also underlined the occurrence of a photoinduced charge separation in which electron-hole pairs are formed during CO_2 reduction by using organic molecules with different oxidation potentials as sacrificial agents [46], the strategy used in the present work. For this, *N,N*-dimethylaniline (0.76 V *vs.* Ag/AgCl) as sacrificial electron donor for photocatalytic CO_2 reduction with RuO_x@UiO-66(Zr/Ce/Ti) resulted in the formation of 253 μmol g^{-1} of CH_4 after 22 h of reaction in simulated sunlight irradiation. In contrast, the use of *p*-xylene with a higher oxidation potential (2.17 V *vs.* Ag/AgCl) as sacrificial electron donor only formed a negligible amount of methane. These results agree with the operation of an LMCT mechanism in which the photogenerated electrons and holes can react with the CO_2 and the sacrificial electron donors, respectively, in this case leading to the formation of methane [46].

To further study how LMCT pathway participated in the reaction mechanism and the associated photocatalytic activity, a comparative study of the RuO_x NPs supported UiO-66 materials was carried out by means of transient absorption spectroscopy in the microsecond time scale by the LFP technique. This is a sensitive tool that can study photoinduced processes such as energy and/or electron transfer, providing valuable information on the transient species formed after excitation, *i.e.* radical anions and/or radical cations, trapped electrons and/or holes [71]. As in the previous PL experiments, LFP was conducted for either fresh or used suspensions of RuO_x NPs supported UiO-66 materials in acetonitrile with the same absorbance (*ca.* 0.4) at the same excitation wavelength (266 nm) to take the different oxidation states of ruthenium into account in both series of samples. Under these conditions, the organic ligand is the main subunit of the whole system excited at 266 nm. In general, LFP spectra of RuO_x@UiO-66 solids under Ar atmosphere are characterized by a continuous absorption band from 300 to 700 nm (Fig. 8a and S27 and S28). Different hole and electron quenchers such as methanol and/or N_2O (or O_2), respectively, were used to study the nature of the different transient species formed. Accordingly, due to the electron donor character of methanol, the transient species absorbing between 300 and 380 nm, assigned to photogenerated holes, were quenched (see Fig. 8a and Figs. S27 and S28). Interestingly, this effect was found to be more important for RuO_x NPs supported on monometallic UiO-66(Zr) and UiO-66(Ce) (Fig. S27a,b and Fig. S28a,b). In contrast, for bimetallic UiO-66(Zr/Ce) or UiO-66(Zr/Ti) (Figs. S27c, d and Fig. S28c,d) and trimetallic UiO-66(Zr/Ce/Ti) (Fig. 8a), almost

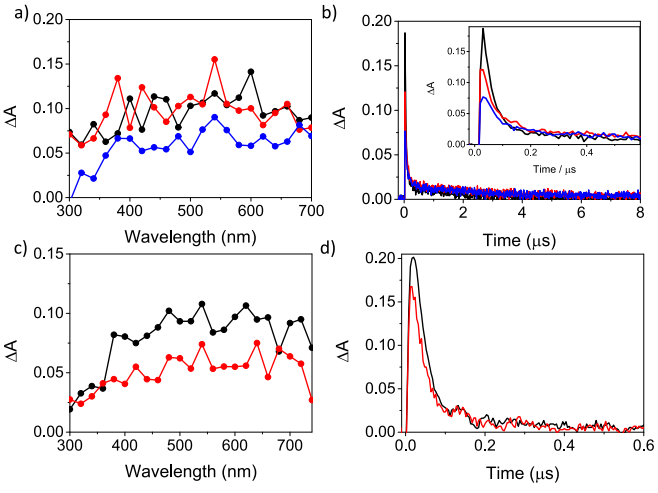

Fig. 8. (a) LFP spectra for fresh RuO_x@UiO-66(Zr/Ce/Ti) under Ar (black), N_2O (red) or under Ar atmosphere in the presence of MeOH (blue line) 50 ns after the laser pulse. (b) Decay traces at 400 nm for fresh RuO_x@UiO-66(Zr/Ce/Ti) under Ar (black), N_2O (red) or under Ar atmosphere in the presence of MeOH (blue). The inset shows the decay traces up to 0.6 μs. (c) LFP spectra for fresh RuO_x@UiO-66(Zr/Ce/Ti) under Ar (black line) or O_2 (red line) atmospheres. (d) Decay traces at 640 nm for fresh RuO_x@UiO-66(Zr/Ce/Ti) under Ar (black line) or O_2 (red line).

quenching was found in the whole spectra from 300 to 700 nm. In addition, for all fresh (Fig. 8b and S29) or used (Fig. S30) samples, methanol mainly quenches the more intense transients, which decayed the fastest in the series, thus supporting the presence of photogenerated holes. In addition, the influence of N_2O as electron acceptor was also studied. As can be seen from Fig. 8a and Figs. S27 and S28, there is a minor influence of N_2O in most of the RuO_x NPs supported UiO-66 solids, where minimal quenching *ca.* 600 nm can be found, especially in UiO-66(Zr/Ce/Ti) supported RuO_x NPs (Fig. 8a). Further quenching experiments using molecular O_2 as electron acceptor were carried out for both fresh and used RuO_x NPs supported in both UiO-66(Zr/Ce/Ti) (Fig. 8c and S32) and UiO-66(Zr) (Fig. S32), since these materials displayed the highest and lowest activity as photocatalysts, respectively. The results show that molecular O_2 quenches different regions of the spectra. In the case of fresh RuO_x NPs supported UiO-66(Zr/Ce/Ti), the regions from about 400 to 700 nm are quenched with a slightly enhanced signal from 300 to 400 nm (Fig. 8c). This is attributed to quenching of the photogenerated electrons (from 400 to 700 nm) and the accumulation of photogenerated holes (from 300 to 400 nm). Molecular O_2 again quenches the more intense signal, decaying faster at 640 nm for both fresh and used RuO_x NPs supported on UiO-66(Zr/Ce/Ti) (Fig. 8d and S33) or UiO-66(Zr) (Fig. S34).

In short, these LFP results from RuO_x NPs supported UiO-66 solid suspensions in acetonitrile in Ar, N_2O and O_2 atmospheres or in the presence of MeOH confirm photoinduced charge separation with the generation of trapped electrons and holes. A comparative study of the transient absorption decay traces at different wavelengths was carried out to further study the influence of RuO_x NPs supported on the mono-, bi- and trimetallic UiO-66 solids. Fig. 9a shows the kinetic traces for the series of fresh RuO_x NPs supported UiO-66 solids recorded at 400 nm. These profiles, together with the above quenching experiments using N_2O/O_2 or MeOH as electron and hole scavengers, respectively, suggest that the fastest and most intense component of the decay trace could be associated with the photoinduced charge separation process, while the component with the second longest lifetime can be attributed to charge delocalization.

To acquire quantitative information on the studied transient species, LFP decays at 400 nm were fitted using a mono- or two-exponential law (see details in the Experimental Section). Table 2 summarizes the lifetimes and percentages of the components obtained for the series of fresh RuO_x NPs supported UiO-66 materials. The results indicate that the fresh UiO-66(Zr) supported RuO_x NPs contributed almost equal amounts of

Table 2
LFP lifetimes and the percentage of each component obtained for the series of fresh RuO_x NPs supported UiO-66 materials. The mean lifetime (<τ>) is also shown.

	τ_1(μs)	Component percentage (%)	τ_2(μs)	Component percentage (%)	<τ>(μs)
RuO_x@UiO-66(Zr)	0.085	48	19.4	52	5.37
RuO_x@UiO-66(Ce)	0.067	92	1.9	8	0.12
RuO_x@UiO-66(Zr/Ce)	0.049	90	2.86	10	0.07
RuO_x@UiO-66(Zr/Ti)	0.062	89	1.85	11	0.11
RuO_x@UiO-66(Zr/Ce/Ti)	0.039	100	–	–	0.04

both long and short decay components and had the higher lifetimes in the series. In contrast, the decay trace for fresh RuO_x@UiO-66(Ce) was dominated by the faster and more intense component (92 %), showing a much shorter lifetime than that of RuO_x@UiO-66(Zr). The corresponding decays of both the bimetallic RuO_x NPs supported UiO-66(Zr/Ce) and UiO-66(Zr/Ti) also mainly exhibited the first component, with τ_1 values somewhat lower than the analogous RuO_x@UiO-66(Ce) sample. Finally, the decay profile of RuO_x@UiO-66(Zr/Ce/Ti), which can be satisfactorily fitted by a single exponential law, provided the fastest decay in the series. Interestingly, the mean lifetimes (<τ >) can be used as an indicator of the photocatalytic activity achieved in this study, the faster the transient absorption decay, the higher the photocatalytic activity. For the series of fresh RuO_x NPs supported UiO-66 solids, the order of fastest kinetics is UiO-66(Zr/Ce/Ti) > UiO-66(Zr/Ce) > UiO-66 (Zr/Ti) > UiO-66(Ce) > UiO-66(Zr) (Table 2). There is also a clear correlation between the average lifetime (Table 1) and photocatalytic activity (Fig. 4). In this regard, the fastest and the lowest average lifetimes detected for both fresh and used UiO-66(Zr/Ce/Ti) and UiO-66 (Zr) supported RuO_x NPs, respectively, were the highest and the lowest observed photocatalytic activity. Similar conclusions can be drawn by using the used UiO-66 solids decorated RuO_x NPs (Fig. S35 and Table S2). These results suggest that RuO_x NPs supported on bimetallic UiO-66(Zr/Ti) and UiO-66(Zr/Ce) solids and specially on the trimetallic UiO-66(Zr/Ce/Ti) favours photoinduced charge carrier separation and delocalization and, thus increasing the resulting photocatalytic activity.

The influence of RuO_x NPs supported on UiO-66(Zr/Ce/Ti) or UiO-

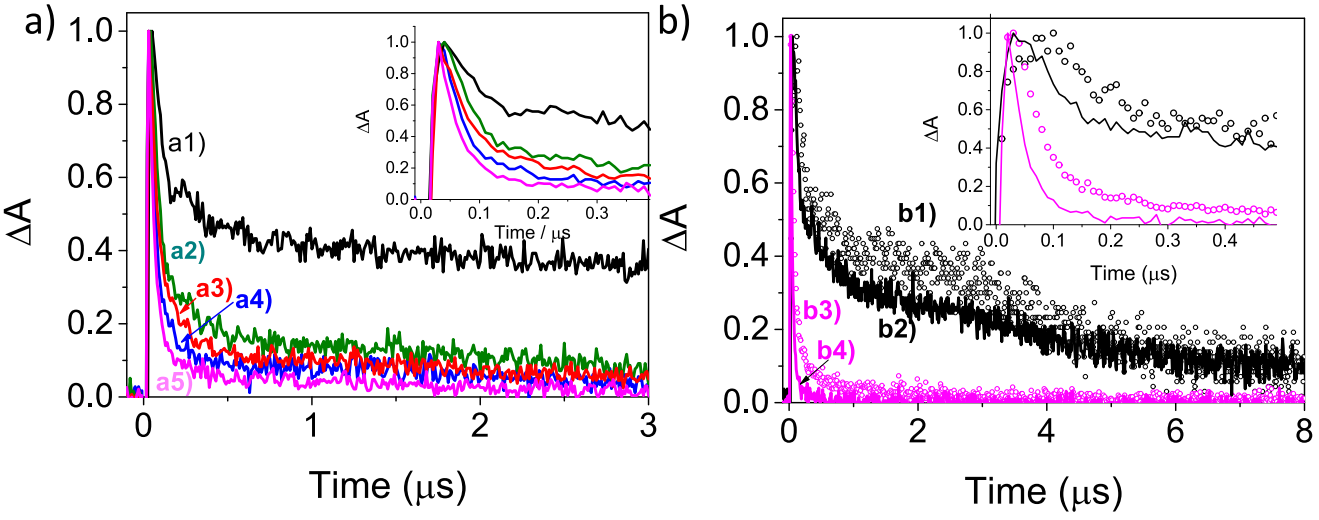

Fig. 9. (a) LFP decay traces (λ_{exc} = 266 nm) at 400 nm for the series of fresh RuO_x NPs supported UiO-66 solids suspended in acetonitrile. Legend: (a1) UiO-66(Zr), (a2) UiO-66(Ce), (a3) UiO-66(Zr/Ce), (a4) UiO-66(Zr/Ti), (a5) UiO-66(Zr/Ce/Ti). (b) LFP decay traces (λ_{exc} = 266 nm) at 400 nm for the series of fresh UiO-66 non-supported with RuO_x NPs. Legend: (b1) UiO-66(Zr), (b2) RuO_x@UiO-66(Zr/Ce/Ti), (b3) UiO-66(Zr/Ce/Ti), (b4) RuO_x@UiO-66(Zr/Ce/Ti).

66(Zr) was further studied on the kinetics of the transient absorption species. Fig. 9b shows that the trimetallic UiO-66(Zr/Ce/Ti) material decayed much faster than UiO-66(Zr) in a similar way to the previously described materials decorated with RuO_x NPs. On the other hand, RuO_x NPs supported on UiO-66(Zr/Ce/Ti) or UiO-66(Zr) in both cases reduced the average lifetimes more than the pristine MOFs. These results indicate that the role of RuO_x NPs favours charge separation and delocalization, both beneficial processes for enhancing photocatalytic activity. Overall, the results further confirm an inverse relationship between the observed transient absorption decays and the photocatalytic activity, the fastest one displaying the highest photocatalytic activity. In a related study, Ma et al. found that for a series of defective UiO-66(Zr)–NH_2 solids supported Pt NPs, the fastest relaxation kinetics were those of the highest photocatalytic activity for H_2 production [72]. These findings highlight the importance of transient absorption spectroscopy for the in-depth understanding and evaluation of the photocatalytic activity achieved when generating solar fuels from H_2O or CO_2.

The above characterization supports the occurrence of a LMCT mechanism that was favoured for bimetallic UiO-66(Zr/Ce) and UiO-66 (Zr/Ti), and especially so for the trimetallic UiO-66(Zr/Ce/Ti), compared with the parent UiO-66(Zr) material, and where the RuO_x NPs also favoured photoinduced charge separation leading to the formation of trapped electrons and holes.

However, based on previous reports [36,38], due to the presence of supported RuO_x NPs, at least part of the observed photocatalytic activity in CO_2 reduction by H_2 at 200 °C is also due to the concurrent appearance of a photothermal reaction pathway. During this mechanism, part of the absorbed light energy is transformed into local heating, especially when using RuO_x NPs with absorption surface plasmon resonance in the visible region of the spectrum [36]. Previous reports proposed that the study of the influence of the light intensity on the resulting photocatalytic activity could be used as indirect evidence to investigate the possibility of operating a photothermal mechanism [36,38]. Fig. 10 shows that there is a quasi-linear relationship between the observed photocatalytic activity for methane generation and the light intensity at irradiances lower than 250 mW/cm^2. This agrees with a photochemical pathway governed by electrons and holes that promote CO_2 reduction and H_2 oxidation reactions, respectively. As the light intensity increases, an exponential relationship with the photogenerated methane can be seen, at least partly characteristic of a photothermal pathway. It should

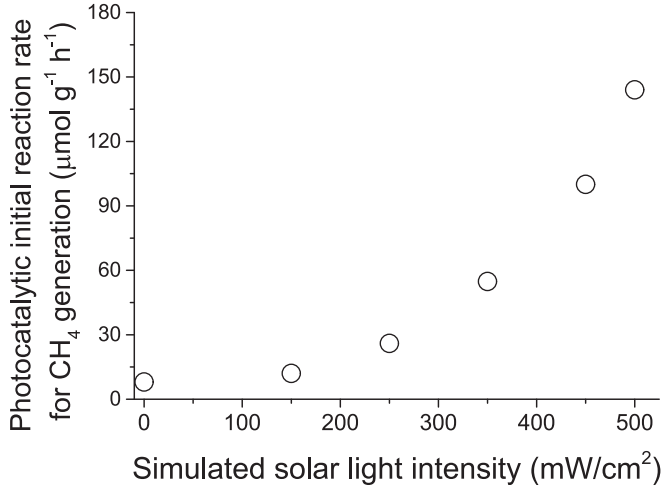

Fig. 10. Photocatalytic initial reaction rate (r_0) for methane production as a function of the simulated solar light intensity using RuO_x@UiO-66(Zr/Ce/Ti). Reaction conditions: Photocatalyst (15 mg), P_{H2} = 1.05 bar, P_{CO2} = 0.25 bar, reaction temperature 200 °C, simulated sunlight irradiation (Hg-Xe lamp of 150 W equipped with an AM 1.5G type filter and the corresponding transmittance filters that decrease the light intensity). Note: The photocatalytic data corresponds to four independent experiments.

be remembered that a previous control experiment with RuO_x@UiO-66 (Zr/Ce/Ti) as catalyst for CO_2 reduction by H_2 at 200 °C gave a methane production of about half (0.037 mmol g^{-1} after 22 h) the production under irradiation (0.082 mmol g^{-1} after 22 h).

Due to all these mechanistic and photocatalytic results, the excellent photocatalytic activity for CO_2 reduction by H_2 with RuO_x@UiO-66(Zr/Ce/Ti) is likely to arise from a dual photochemical and photothermal reaction pathway. Based on the acquired acknowledge in the literature [11,22,26,27,30,37], together with the photodeposition method, photocurrent data, LFP and PL measurements and photocatalytic results, suggests that RuO_x@UiO-66(Zr/Ce/Ti) operates at least in part via a photoinduced electron transfer pathway from the HOCO of terephthalate organic ligand to the LUCO present in the metal node (Fig. 11). The electrons would then be transferred to RuO_x NPs, where selective reduction of CO_2 to CH_4 occurs. *In situ* FT-IR spectroscopy using CO as probe molecule indicates that the role of RuO_x NPs in favouring CO_2 intermediate chemisorption and selective CH_4 formation. RuO_x NPs supported UiO-66(Zr/Ce/Ti) also favours CO_2 reduction to CH_4 via a photothermal mechanism by converting light energy into heat. Fig. 11 shows the proposed photochemical and photothermal reaction pathways that can take place during the photocatalytic CO_2 reduction to CH_4 using RuO_x@UiO-66(Zr/Ce/Ti).

4. Conclusions

In summary, this study proposes on the development of highly active photocatalysts based on mixed-metal UiO-66 solids supported small RuO_x NPs (1 wt%; ~1.46 nm) for CO_2 methanation by H_2 at 200 °C under simulated sunlight irradiation. Based on previous precedents, the initial hypothesis of our investigation was that the photocatalytic activity of monometallic UiO-66(Zr) supported RuO_x NPs can be enhanced by preparing mixed-metal UiO-66 solids with Ti(IV) and/or Ce(IV) ions. UiO-66(Zr/Ti/Ce) decorated with RuO_x NPs was the most active photocatalyst in the series, followed by their analogous bimetallic UiO-66 (Zr/Ti) or UiO-66(Zr/Ce) and monometallic UiO-66(Zr) and UiO-66 (Ce). The photocatalytic activity of RuO_x@UiO-66(Zr/Ce/Ti) depends on the reaction temperature according to the Arrhenius law and has an apparent activation energy of 29 kJ/mol. The photocatalytic activity achieved by RuO_x@UiO-66(Zr/Ce/Ti) (1900 μmol g^{-1} after 22 h) ranks this material among the most active analogous MOF-based photocatalysts used for the same purpose [36,46]. The photocatalyst can be reused several times without undergoing any reduction in its activity while maintaining its crystallinity and morphology, as indicated by PXRD and SEM measurements. The photocatalytic and spectroscopic experiments support the outstanding photocatalytic activity of RuO_x@UiO-66(Zr/Ce/Ti) through a dual photothermal and photochemical reaction mechanism. The innovation of this research is that proposes to implement the concept of mixed-metal MOFs such as UiO-66 (Zr/Ce/Ti) decorated with RuO_x NPs to boost the photocatalytic activity for the selective gas-phase CO_2 methanation by H_2 under simulated sunlight irradiation.

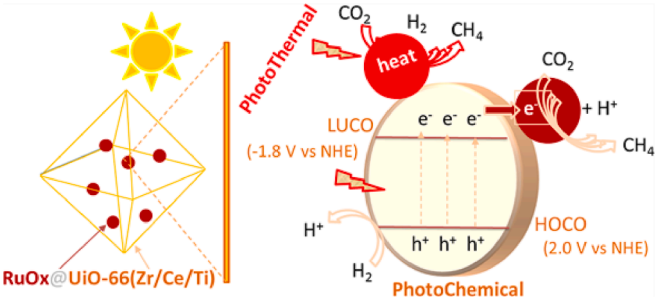

Fig. 11. Proposed reaction mechanism during the photocatalytic CO_2 reduction by H_2 using RuO_x@UiO-66(Zr/Ce/Ti).

The authors envision that this study will pave the way towards new research in the development of efficient mixed-metal MOFs as photocatalysts for solar-driven CO_2 reduction.

Declaration of Competing Interest

The authors declare that they have no known competing financial interests or personal relationships that could have appeared to influence the work reported in this paper.

Data availability

Data will be made available on request.

Acknowledgements

Grant FPU20/03140 funded by MCIN/mAEI/ 10.13039/501100011033 ESF Investing in your future. I.V. thanks the support of grant PID2020-115010RB-I00 funded by MCIN/AEI/10.13039/501100011033. S.N. thanks the support of grant PID2021-123856OB-I00 funded by MCIN/AEI/ 10.13039/501100011033 and by ERDF A way of making Europe. S.N acknowledges the funding for open access charge from "CRUE-Universitat Politècnica de València."

Appendix A. Supplementary data

Supplementary data to this article can be found online at https://doi.org/10.1016/j.cej.2023.143553.

References

[1] K. Bosa, J. Gupta, Stranded assets and stranded resources: implications for climate change mitigation and global sustainable development, Energy Res. Soc. Sci. 56 (2019), 101215, https://doi.org/10.1016/j.erss.2019.05.025.
[2] H. Lin, S. Luo, H. Zhang, J. Ye, Toward solar-driven carbon recycling, Joule 6 (2022) 294–314.
[3] S. Safarian, R. Unnthorsson, C. Richter, Effect of coronavirus disease 2019 on CO2 emission in the world, Aerosol Air Qual. Res. 20 (2020) 1197–1203.
[4] S. Paraschiv, L.S. Paraschiv, Trends of carbon dioxide (CO2) emissions from fossil fuels combustion (coal, gas and oil) in the EU member states from 1960 to 2018, Energy Rep. 6 (2020) 237–242.
[5] R. Shahnazi, Z.D. Shabani, The effects of renewable energy, spatial spillover of CO2 emissions and economic freedom on CO2 emissions in the EU, Renew. Energy 169 (2021) 293–307.
[6] M. Tayyab, Y. Liu, Z. Liu, Z. Xu, W. Yue, L. Zhou, J. Lei, J. Zhang, A new breakthrough in photocatalytic hydrogen evolution by amorphous and chalcogenide enriched cocatalysts, Chem. Eng. J. 445 (2023), 140601.
[7] Z. Ye, W. Yue, M. Tayyab, J. Zhang, J. Zhang, Simple one-pot, high-yield synthesis of 2D graphitic carbon nitride nanosheets for photocatalytic hydrogen production, Dalton Trans. 51 (2022) 18542–18548.
[8] M. Danish, M. Tayyab, A. Akhtar, A.A. Altaf, S. Kausar, S. Ullah, M. Iqbal, Effect of soft template variation on the synthesis, physical, and electrochemical properties of Mn3O4 nanomaterial, Inorg. Nano-Met. Chem. 51 (2020) 359–365.
[9] G. Liu, M. Feng, M. Tayyab, J. Gong, M. Zhang, M. Yang, K. Lin, Direct and efficient reduction of perfluorooctanoic acid using bimetallic catalyst supported on carbon, J. Hazard. Mater. 412 (2021), 125224.
[10] Y. Liu, Q. Zhu, M. Tayyab, L. Zhou, J. Lei, J. Zhang, Single-atom Pt loaded zinc vacancies ZnO-ZnS induced type-V electron transport for efficiency photocatalytic H2 evolution, Solar RRL 5 (2021) 2100536.
[11] M. Tayyab, Y. Liu, Z. Liu, L. Pan, Z. Xu, W. Yue, L. Zhou, J. Lei, J. Zhang, One-pot in-situ hydrothermal synthesis of ternary In2S3/Nb2O5/Nb2C Schottky/S-scheme integrated heterojunction for efficient photocatalytic hydrogen production, J. Colloid Interface Sci. 628 (2022) 500–512.
[12] M. Tayyab, Y. Liu, S. Min, R. Muhammad Irfan, W. Zhu, L. Zhou, J. Lei, J. Zhang, Simultaneous hydrogen production with the selective oxidation of benzyl alcohol to benzaldehyde by a noble-metal-free photocatalyst VC/CdS nanowires, Chin. J. Catal. 43 (2022) 1165–1175.
[13] P. Friedlingstein, M. O'Sullivan, M.W. Jones, R.M. Andrew, J. Hauck, A. Olsen, G. P.P. Peters, W. Peters, J. Pongratz, S. Sitch, C. Le Quéré, J.G. Canadell, P. Ciais, R. B. Jackson, S. Alin, L.E.O.C. Aragão, A. Arneth, V. Arora, N.R.R. Bates, M. Becker, A. Benoit-Cattin, H.C.C. Bittig, L. Bopp, S. Bultan, N. Chandra, F. Chevallier, L. P. Chini, W. Evans, L. Florentie, P.M. Forster, T. Gasser, M. Gehlen, D. Gilfillan, T. Gkritzalis, L. Gregor, N. Gruber, I. Harris, K. Hartung, V. Haverd, R.A. Hughton, T. Ilyina, A.K. Jain, E. Joetzjer, K. Kadono, E. Kato, V. Kitidis, J.I. Korsbakken, P. Landschützer, N. Lefèvre, A. Lenton, S. Lienert, Z. Liu, D. Lombardozzi, G. Marland, N. Metzl, D.R. Munro, J.E.M.S. Nabel, S.-I. Nakaoka, Y. Niwa, K. O'Brien, T. Ono, P.I. Palmer, D. Pierrot, B. Poulter, L. Resplandy, E. Robertson, C. Rödenbeck, J. Schwinger, R. Séférian, I. Skjelvan, A.J.P. Smith, A.J. Sutton, T. Tanhua, P. Tans, H. Tian, B. Tilbrook, G. van der Werf, N. Vuichard, A.P. Walker, R. Wanninkhof, A.J. Watson, D. Willis, A.J. Wiltshire, W. Yuan, X. Yue, S. Zaehle, Global carbon budget, Earth Syst. Sci. Data 12 (2020) 3269–3340.
[14] W. Gao, S. Liang, R. Wang, Q. Jiang, Y. Zhang, Q. Zhen, B. Xi, C.Y. Ying To, X. Zhu, J. Wang, L. Huang, Y. Gao, Z. Wang, C. Jo, Q. Wang, L. Wang, Y. Liu, B. Louis, J. Scott, A.-C. Roger, R. Amal, H. He, S.-e. Park, Industrial carbon dioxide capture and utilization: state of the art and future challenges, Chem. Soc. Rev. 49 (2020) 8584–8686.
[15] M. Radovanović, S. Filipović, S. Vukadinović, M. Trbojević, I. Podbregar, Decarbonisation of eastern EUROPEAN economies: monitoring, economic, social and security concerns, Energy Sustain. Soc. 12 (2022) 16.
[16] K. de Kleijne, S.V. Hanssen, L. van Dinteren, M.A.J. Huijbregts, R. van Zelm, H. de Coninck, Limits to Paris compatibility of CO2 capture and utilization, One Earth 5 (2022) 168–185.
[17] P. Markewitz, W. Kuckshinrichs, W. Leitner, J. Linssen, P. Zapp, R. Bongartz, A. Schreiber, T.E. Müller, Worldwide innovations in the development of carbon capture technologies and the utilization of CO2, Energy Environ. Sci. 5 (2012) 7281–7305.
[18] M. Mikkelsen, M. Jørgensen, F.C. Krebs, The teraton challenge. a review of fixation and transformation of carbon dioxide, Energy Environ. Sci. 3 (2010) 43–81.
[19] Z. Zhang, S.-Y. Pan, H. Li, J. Cai, A.G. Olabi, E.J. Anthony, V. Manovic, Recent advances in carbon dioxide utilization, Renewable Sustainable Energy Rev. 125 (2020), 109799.
[20] J. Artz, T.E. Müller, K. Thenert, J. Kleinekorte, R. Meys, A. Sternberg, A. Bardow, W. Leitner, Sustainable conversion of carbon dioxide: an integrated review of catalysis and life cycle assessment, Chem. Rev. 118 (2018) 434–504.
[21] A.J. Kamphuis, F. Picchioni, P.P. Pescarmona, CO2-fixation into cyclic and polymeric carbonates: principles and applications, Green Chem. 21 (2019) 406–448.
[22] M. Younas, L.L. Loong Kong, M.J.K. Bashir, H. Nadeem, A. Shehzad, S. Sethupathi, Recent advancements, fundamental challenges, and opportunities in catalytic methanation of CO2, Energy Fuels 30 (2016) 8815–8831.
[23] M.A.A. Aziz, A.A. Jalil, S. Triwahyono, A. Ahmad, CO2 methanation over heterogeneous catalysts: recent progress and future prospects, Green Chem. 17 (2015) 2647–2663.
[24] S. Walspurger, W.G. Haije, B. Louis, CO2 reduction to substitute natural gas: toward a global low carbon energy system, Isr. J. Chem. 54 (2014) 1432–1442.
[25] S. Mathur, G. Gosnell, B.K. Sovacool, D.D.F. Del Rioade, S. Griffiths, M. Bazilian, J. Kim, Industrial decarbonization via natural gas: a critical and systematic review of developments, socio-technical systems and policy options, Energy Res. Soc. Sci. 90 (2022), 102638.
[26] J. Albero, Y. Peng, H. García, Photocatalytic CO2 reduction to C2+ products, ACS Catal. 10 (2020) 5734–5749.
[27] S. Khan, X. Dai, T. Ali, S. Mahmood, M. ul Haq, M. Sohail Riaz, Y. Hu, Recent advances on photo-thermo-catalysis for carbon dioxide methanation, Int. J. Hydrog. Energy (2022).
[28] K.R. Thampi, J. Kiwi, M. Graetzel, Methanation and photo-methanation of carbondioxide at room-temperature and atmospheric-pressure, Nature 327 (1987) 506–508.
[29] D. Wang, J. Huang, F. Liu, X. Xu, X. Fang, J. Liu, Y. Xie, X. Wang, Rutile RuO2 dispersion on rutile and anatase TiO2 supports: the effects of support crystalline phase structure on the dispersion behaviors of the supported metal oxides, Catal. Today 339 (2020) 220–232.
[30] D. Mateo, J. Albero, H. García, Photoassisted methanation using Cu2O nanoparticles supported on graphene as a photocatalyst, Energy Environ. Sci. 10 (2017) 2392–2400.
[31] D. Mateo, J. Albero, H. García, Graphene supported NiO/Ni nanoparticles as efficient photocatalyst for gas phase CO2 reduction with hydrogen, Appl. Catal. B.-Environ. 224 (2018) 563–571.
[32] J. Barrio, D. Mateo, J. Albero, H. García, M. Shalom, A heterogeneous carbon nitride–nickel photocatalyst for efficient low-temperature CO2 methanation, Adv. Energy Mater. 9 (2019) 1902738.
[33] D. Mateo, J. Albero, H. Garcıa, Titanium-perovskite-supported RuO2 nanoparticles for photocatalytic CO2 methanation, Joule 3 (2019) 1949–1962.
[34] M. Cabrero-Antonino, S. Remiro-Buenamañana, M. Souto, A.A. García-Valdivia, D. Choquesillo-Lazarte, S. Navalón, A. Rodríguez-Diéguez, G. Mínguez-Espallargas, H. García, Design of cost-efficient and photocatalytically active Zn-based MOFs decorated with Cu2O nanoparticles for CO2 methanation, Chem. Commun. 55 (2019) 10932–10935.
[35] A.A. Jelle, K.K. Ghuman, P.G. O'Brien, M. Hmadeh, A. Sandhel, C.D.D. Perovic, V. Singh, C.A. Mims, G.A. Ozin, Highly efficient ambient temperature CO2 photomethanation catalyzed by nanostructured RuO2 on silicon photonic crystal support, Adv. Energy Mater. 8 (2018) 1702277.
[36] M. Cabrero-Antonino, B. Ferrer, H.G. Baldoví, S. Navalón, Toward solar-driven photocatalytic CO2 methanation under continuous flow operation using benchmark MIL-125(Ti)-NH2 supported ruthenium nanoparticles, Chem. Eng. J. 445 (2022), 136426.
[37] I.S. Khan, L. Garzon-Tovar, D. Mateo, J. Gascon, Metal-organic-frameworks and their derived materials in photo-thermal catalysis, Eur. J. Inorg. Chem. 28 (2022) e202200316.
[38] D. Mateo, J.L. Cerrillo, S. Durini, J. Gascon, Fundamentals and applications of photo-thermal catalysis, Chem. Soc. Rev. 50 (2021) 21732210.
[39] G. Férey, C. Mellot-Draznieks, C. Serre, F. Millange, J. Dutour, S. Surblé, I. Margiolaki, A chromium terephthalate-based solid with unusually large pore volumes and surface area, Science 23 (2005) 2040–2042.

[40] H. Furukawa, K.E. Cordova, M. O'Keeffe, O.M. Yaghi, The chemistry and applications of metal-organic frameworks, Science 341 (2013) 1230444.
[41] S. Kitagawa, R. Kitaura, S.-I. Noro, Functional porous coordination polymers, Angew. Chem. Int. Ed. 43 (2004) 2334–2375.
[42] A. Dhakshinamoorthy, A.M. Asiri, H. García, Metal-organic framework (MOF) compounds: photocatalysts for redox reactions and solar fuel production, Angew. Chem. Int. Ed. 55 (2016) 5414–5445.
[43] A. Dhakshinamoorthy, Z. Li, H. Garcia, Catalysis and photocatalysis by metal organic frameworks, Chem. Soc. Rev. 47 (2018) 8134–8172.
[44] Y. Yan, C. Li, Y. Wu, J. Gao, Q. Zhang, From isolated Ti-oxo clusters to infinite Ti-oxo chains and sheets: recent advances in photoactive Ti-based MOFs, J. Mater. Chem. A 8 (2020) 15245–15270.
[45] J. Zhu, P.-Z. Li, W. Guo, Y. Zhao, R. Zou, Titanium-based metal–organic frameworks for photocatalytic applications, Coord. Chem. Rev. 359 (2018) 80–101.
[46] S. Wang, M. Cabrero-Antonino, S. Navalón, C.-C. Chen-chen Cao, A. Tissot, I. Dovgaliuk, J. Marrot, C. Martineau-Corcos, L. Yu, H. Wang, W. Shepard, H. García, C. Serre, A robust titanium isophthalate metal-organic framework for visible-light photocatalytic CO2 methanation, Chem 6 (2020) 3409–3427.
[47] R. Li, W. Zhang, K. Zhou, Metal–organic-framework-based catalysts for photoreduction of CO2, Adv. Mater. 30 (2018) 1705512.
[48] R. Jaryal, R. Kumar, S. Khullar, Mixed metal-metal organic frameworks (MM-MOFs) and their use as efficient photocatalysts for hydrogen evolution from water splitting reactions, Coord. Chem. Rev. 464 (2022), 214542.
[49] H. Liu, M. Cheng, Y. Liu, G. Zhang, L. Li, L. Du, B. Li, S. Xiao, G. Wang, X. Yang, Modified UiO-66 as photocatalysts for boosting the carbon-neutral energy cycle and solving environmental remediation issues, Coord. Chem. Rev. 458 (2022), 214428.
[50] A. Bhattacharyya, M. Gutiérrez, B. Cohen, A. Valverde-González, M. Iglesias, A. Douhal, How does the metal doping in mixed metal MOFs influence their photodynamics? a direct evidence for improved photocatalysts, Mater. Today Energy 29 (2022), 101125.
[51] A. Melillo, M. Cabrero-Antonino, S. Navalón, M. Alvaro, B. Ferrer, H. García, Enhancing visible light photocatalytic activity for overall water splitting in UiO-66 by controlling metal node composition, Appl. Catal. B. Environ. 278 (2020), 119345.
[52] X.-P. Wu, L. Gagliardi, D.G. Truhlar, Metal doping in cerium metal-organic frameworks for visible-response water splitting photocatalysts, J. Chem. Phys. 150 (2019), 041701.
[53] D. Sun, W. Liu, M. Qiu, Y. Zhang, Z. Li, Introduction of a mediator for enhancing photocatalytic performance via post-synthetic metal exchange in metal–organic frameworks (MOFs), Chem. Commun. 51 (2015) 2056–2059.
[54] A. Santiago-Portillo, H.G. Baldoví, M.T. García Fernandez, S. Navalón, P. Atienzar, B. Ferrer, M. Alvaro, H. Garcia, Z. Li, Ti as mediator in the photoinduced electron transfer of mixed-metal NH2−UiO-66(Zr/Ti): transient absorption spectroscopy study and application in photovoltaic cell, J. Phys. Chem. C 121 (2017) 7015–7024.
[55] X.-P. Wu, L. Gagliardi, D.G. Truhlar, Cerium metal−organic framework for photocatalysis, J. Am. Chem. Soc. 140 (2018) 7904–7912.
[56] S. Dai, E. Montero-Lanzuela, A. Tissot, H.G. Baldoví, H. García, S. Navalón, C. Serre, Room temperature design of Ce(IV)-MOFs: from photocatalytic HER and OER to overall water splitting under simulated sunlight irradiation, Chem. Sci. 14 (2023) 3451–3461.
[57] C. Vallés-García, E. Gkaniatsou, A. Santiago-Portillo, M. Giménez-Marqués, M. Álvaro, J.-M. Greneche, N. Steunou, C. Sicard, S. Navalón, C. Serre, H. García, Design of stable mixed-metal MIL-101(Cr/Fe) materials with enhanced catalytic activity for the Prins reaction, J. Mater. Chem. A 8 (2020) 17002–17011.
[58] W. Hou, C. Chen, D. Xie, Y. Xu, Substituted Ti(IV) in Ce-UiO-66-NH2 metal−organic frameworks increases H2 and O2 evolution under visible light, ACS Appl. Mater. Interfaces 15 (2023) 2911–2921.
[59] J.H. Cavka, S. Jakobsen, U. Olsbye, N. Guillou, C. Lamberti, S. Bordiga, K. Lillerud, A new zirconium inorganic building brick forming metal organic frameworks with exceptional stability, J. Am. Chem. Soc. 130 (2008) 13850–13851.
[60] M. Stawowy, M. Róziewicz, E. Szczepanska, J. Silvestre-Albero, M. Zawadzki, M. Musioł, R. Łuzny, J. Kaczmarczyk, J. Trawczynski, A. Łamacz, The impact of synthesis method on the properties and CO2 sorption capacity of UiO-66(Ce), Catalysts 9 (2019) 309.
[61] T.P.L. Giang, T.N.M. Tran, X.T. Le, Preparation and characterization of titanium dioxide nanotube array supported hydrated ruthenium oxide catalysts, Adv. Nat. Sci.-Nanosci. Nanotechnol. 3 (2012), 015008.
[62] D.J. Morgan, Resolving ruthenium: XPS studies of common ruthenium materials, Surf. Interface. Anal. 47 (2015) 1072–1079.
[63] X. Qiu, Y. Zhu, X. Zhang, Y. Zhang, L.T. Menisa, C. Xia, S. Liu, Z. Tang, Cerium-based metal–organic frameworks with UiO architecture for visible light-induced aerobic oxidation of benzyl alcohol, Solar RRL 4 (2020) 1900449.
[64] C.M. Rueda-Navarro, B. Ferrer, H.G. Baldoví, S. Navalon, Photocatalytic hydrogen production from glycerol aqueous solutions as sustainable feedstocks using Zr-based UiO-66 materials under simulated sunlight irradiation, Nanomaterials 12 (2022) 3808.
[65] P. Parnicka, W. Lisowski, T. Klimczuk, A. Mikolajczyk, A. Zaleska-Medynska, A novel (Ti/Ce)UiO-X MOFs@TiO2 heterojunction for enhanced photocatalytic performance: boosting via Ce4+/Ce3+ and Ti4+/Ti3+ redox mediators, Appl. Catal. B. Environ. 310 (2022), 121349.
[66] S. Kattel, P. Liu, J.G. Chen, Tuning selectivity of CO2 hydrogenation reactions at the metal/oxide interface, J. Am. Chem. Soc. 139 (2017) 9739–9754.
[67] S.Y. Chin, C.T. Williams, M.D. Amiridis, FTIR Studies of CO Adsorption on Al2O3- and SiO2-Supported Ru Catalysts, J. Phys. Chem. B 110 (2006) 871–882.
[68] K. McCullough, P.-H. Chiang, J.D. Jimenez, J.A. Lauterbach, Material discovery and high throughput exploration of Ru based catalysts for low temperature ammonia decomposition, Materials 13 (2020) 1869.
[69] A. De Vos, K. Hendrickx, P. Van Der Voort, V. Van Speybroeck, K. Lejaeghere, Missing linkers: an alternative pathway to UiO-66 electronic structure engineering, Chem. Mater. 29 (2017) 3006–3019.
[70] K. Hendrickx, D.E.P. Vanpoucke, K. Leus, K. Lejaeghere, A.V. Van Yperen-De Deyne, V. Van Speybroeck, P. Van Der Voort, K. Hemelsoet, Understanding intrinsic light absorption properties of UiO-66 frameworks: a combined theoretical and experimental study, Inorg. Chem. 54 (2015) 10701–10710.
[71] M.E. El-Khouly, E. El-Mohsnawy, S. Fukuzumi, Solar energy conversion: from natural to artificial photosynthesis, J. Photochem. Photobiol. C 31 (2017) 36–83.
[72] X. Ma, L. Wang, Q. Zhang, H.-L. Jiang, Switching on the photocatalysis of metal–organic frameworks by engineering structural defects, Angew. Chem. Int. Ed. 58 (2019) 12175–12179.